### **Research Article**

Song Yang, Guangjin Zhang, and Guoqing Xiao\*

# Parameter optimization for ultrasonic-assisted grinding of γ-TiAl intermetallics: A gray relational analysis approach with surface integrity evaluation

https://doi.org/10.1515/rams-2024-0045 received April 03, 2024; accepted July 08, 2024

**Abstract:** The processing of y-TiAl intermetallic compound (Ti-45Al-2Mn-2Nb) is essential for manufacturing aircraft engine components, known for their challenging machinability. This study delved into the machining performance of y-TiAl intermetallic compound through ultrasonically assisted grinding experiments. Various grinding parameters, such as wheel rotation speed  $(v_s)$ , feed rate  $(v_w)$ , depth of grinding  $(a_p)$ , and ultrasonic amplitude (A), were investigated to understand their effects on grinding forces, temperatures, and surface quality. Gray relational analysis (GRA) and analysis of variance were used to analyze experimental data and ascertain the optimal machining parameters for ultrasonically assisted grinding of y-TiAl intermetallic compound. Additionally, post-processing surface integrity, encompassing surface roughness, morphology, and residual stresses, was evaluated. The optimal grinding parameter combination was determined as  $F_n = 3.22 \text{ N}$ ,  $F_t = 1.08 \text{ N}$ , and  $T = 174 ^{\circ}\text{C}$  through GRA. Under the selected machining conditions, the depth of cut exerted the most significant influence on the grinding force and temperature, while the effect of wheel speed was the weakest. The surface roughness (Ra) of the workpiece increased with increasing feed rate and depth of the cut but decreased gradually with increasing wheel speed. Upon applying ultrasonic vibration, there was a notable decrease in surface roughness, ranging from 20.12 to 7.67%. However, the increase in the wheel speed, depth of cut, and feed rate inhibited the reduction of roughness due to ultrasonic vibration. Ultrasonic vibration effectively reduced the profile height of the workpiece surface, with a maximum reduction of 1.94  $\mu m$  within the selected range. Nonetheless, as the wheel speed, depth of cut, and feed rate increased, the effectiveness of this reduction gradually diminished.

**Keywords:** γ-TiAl intermetallics, ultrasound-assisted grinding, GRA, surface integrity

### 1 Introduction

 $\gamma$ -TiAl intermetallics are highly regarded as ideal materials for high-temperature applications due to their exceptional resistance to high temperatures [1–3]. These materials have garnered significant attention as promising candidates for manufacturing hot-end components in next-generation commercial aircraft engines, owing to their superior mechanical properties such as outstanding creep resistance, high-temperature strength, antioxidant properties, and lower density [4,5]. Consequently,  $\gamma$ -TiAl intermetallics are extensively used in producing crucial aircraft engine components like low-pressure turbine blades, high-pressure compressors, and charging turbines, with great anticipation for their performance in real-world applications [6–8].

 $\gamma$ -TiAl intermetallics demonstrate exceptional mechanical and chemical properties, as evidenced in Table 1 [9–12]. Compared to other titanium aluminide alloys, they possess higher specific strength, greater hardness, an elevated elastic modulus, and enhanced resistance to high-temperature creep and oxidation. Despite their density being 50% lower than that of nickel-based superalloys,  $\gamma$ -TiAl intermetallics can operate within the 750–900°C range, similar to nickel-based alloys. This operational range is facilitated by the formation of a dense oxide film on their surface at elevated temperatures, effectively preventing further oxidation and combustion and conferring outstanding fire resistance. Moreover, the significantly higher stiffness of

**Guangjin Zhang:** School of Mechanical and Power Engineering, Henan Polytechnic University, Jiaozuo, 454000, China, e-mail: zhangguangjin0824@163.com

<sup>\*</sup> Corresponding author: Guoqing Xiao, School of Mechanical and Power Engineering, Henan Polytechnic University, Jiaozuo, 454000, China, e-mail: xgq77923@163.com

**Song Yang:** School of Software, Henan Polytechnic University, Jiaozuo, 454000, China, e-mail: 2682139520@qq.com

Table 1: Comparison of mechanical properties of y-TiAl intermetallics with other high-temperature alloys

| Performance  | y-TiAl        | Ti <sub>2</sub> AlNb | α <sub>2</sub> -Ti <sub>3</sub> Al | TC4           | Superalloy    |
|--|---------------|----------------------|------------------------------------|---------------|---------------|
| Density (g·cm <sup>-3</sup> )                              | 3.7-3.9       | 5-5.8                | 4.1-4.7                            | 4.54          | 8~8.68        |
| Elastic modulus (GPa)                                      | 160-180       | 102-134              | 110-145                            | 96-110        | 206~207       |
| Yield strength (MPa)                                       | 400-800       | 1,030-1,292          | 700-1,150                          | 380-1,150     | 800-1,260     |
| Tensile strength (MPa)                                     | 450-900       | 1,245-1,413          | 750-1,200                          | 480-1,200     | 1,250-1,450   |
| Room temperature ductility (%)                             | 1–4           | 3.5-10               | 2–10                               | 5–20          | 3–10          |
| High temperature plasticity (%)                            | 10-60 (870°C) | 6-14 (650°C)         | 10-20 (660°C)                      | 15-50 (550°C) | 10-20 (870°C) |
| Room-temperature fracture toughness (MPa·m <sup>-2</sup> ) | 12-35         | 39                   | 12-80                              | 52            | 30-100        |
| Antioxidant limit (°C)                                     | 800-950       | 1,100                | 650                                | 600           | 870-1,093     |
| Thermal conductivity $(W\cdot(m\cdot K)^{-1})$             | 22-24         | 7.87                 | 7                                  | 6.8-7.95      | 13.4          |
| Expansion coefficient (10 <sup>-6</sup> ·K <sup>-1</sup> ) | 10.8          | 8.22                 | 10                                 | 9.1           | 11.8          |

 $\gamma$ -TiAl intermetallics enables them to meet the stringent requirements for precision components characterized by high strength and low spacing. Additionally, they exhibit commendable resistance to high-temperature creep, maintaining optimal performance even at temperatures ranging from 600 to 700°C. Consequently, these advantageous properties position  $\gamma$ -TiAl intermetallics as promising lightweight high-temperature alloy materials, aptly satisfying the high-performance demands of critical components such as high-pressure blades in aerospace engines, mid- and low-pressure blades in gas turbines, and stator vanes in compressors. As a result, the widespread recognition of  $\gamma$ -TiAl intermetallics underscores their significant potential for development as lightweight, high-temperature alloy materials.

Grinding is a crucial precision machining technique, particularly suitable for processing materials with high strength, toughness, and difficulty in machining [13]. It involves the use of abrasive particles to remove material from a workpiece, typically achieved by rotating a grinding wheel against the workpiece surface to achieve high surface quality [14,15]. Researchers have conducted relevant grinding studies on y-TiAl. Hood et al. [16] conducted precision machining on γ-TiAl alloys using single-layer electroplated diamond grinding wheels. They effectively removed hardening layers up to 625 HK induced by rough machining, achieving a surface roughness (Ra) of less than 0.3 µm, significantly below the values required for aerospace components. Conventional grinding typically ensures machining quality by limiting process parameters, which can lead to uncertain machining efficiency. Xi et al. [17] evaluated the performance of creep feed grinding y-TiAl using electroplated diamond grinding wheels. They demonstrated superior grinding effectiveness and lower wheel wear rates, achieving a maximum material removal rate of 12 mm<sup>3</sup>·(mm·s)<sup>-1</sup>, compared to approximately half for cubic boron nitride (CBN) wheels. Chen et al. [18] analyzed the evolution of surface integrity of y-TiAl (y titanium aluminide) intermetallics using creep feed profile grinding (CFPG). Their analysis showed that

the contour features of blade tenons significantly influence the processed surface integrity formed by thermal-mechanical effects. This influence is particularly evident in the different surface roughness, metallographic structures, microhardness, and residual stresses observed at various inspection locations. However, conventional grinding (CG) often encounters challenges such as high grinding force and temperature when applied to  $\gamma$ -TiAl intermetallics, leading to various defects like adhesion, cracks, residual tensile stress, or thermal burns [19–22].

Several researchers have investigated the benefits of ultrasound-assisted machining techniques in reducing machining forces and improving machining quality. For instance, Jamshidi and Nategh [23] explored the frictional behavior at the tool-chip interface during ultrasound-assisted turning (UAT) and developed a mathematical model to elucidate UAT's effects in reducing normal force and friction. Yang et al. [24] simulated machined surfaces obtained through ultrasonic vibration-assisted grinding (UVAG), observing unique texture features induced by ultrasonic vibration. Zhao et al. [25] proposed a novel UVAG process that significantly reduced grinding force and heat generation. Cao et al. [26] analyzed material removal mechanisms in UVAG and observed substantial reductions in grinding force and temperature, along with improved surface quality. These studies highlight the potential of ultrasonic-assisted techniques in enhancing machining processes for various materials, including brittle ones.

Despite extensive research on high-speed grinding of  $\gamma$ -TiAl intermetallics using diamond grinding wheels, focusing on tool wear and material removal mechanisms, limited attention has been paid to comprehensive assessments of surface integrity parameters like microcracks, residual stress, sub-surface hardness, and chip morphology after high-efficiency precision grinding. The optimization of grinding parameters through statistical methods such as orthogonal experimental design and gray relational analysis (GRA) has shown promise in enhancing grinding processes [27–29]. However, there remains a gap in theoretical

and systematic analyses of parameter optimization to derive objective and comprehensive conclusions for informed decision-making.

To bridge these gaps and enhance the grinding quality of y-TiAl intermetallics, we conducted ultrasound-assisted grinding experiments optimized through GRA. Our study aimed to determine the optimal grinding parameters for achieving improved surface integrity, including surface roughness, morphology, and residual stress, in y-TiAl intermetallics machining.

### 2 Materials and methods

### 2.1 Experimental setup

Prior to commencing the ultrasonic-assisted grinding of y-TiAl intermetallic compounds, it is essential to introduce the instrumentation required for the experiments and provide an overview of the properties of  $\gamma$ -TiAl intermetallics. This section, therefore, offers an introduction to the experimental setup for ultrasonic-assisted grinding of y-TiAl intermetallic compounds, along with an overview of the properties of y-TiAl intermetallic compounds. Furthermore, a description of the processing parameters employed in the experiments is provided.

Grinding is a commonly used metal processing method. It involves removing material from the workpiece surface through the relative motion between an abrasive and the workpiece, resulting in precise dimensions and a smooth finish. However, certain materials, such as y-TiAl intermetallic compounds, present machining challenges. These challenges can lead to severe tool wear and decreased surface quality. To overcome these obstacles, ultrasonically assisted machining has emerged. This technique uses ultrasonic vibration to enhance cutting conditions during grinding. By doing so, it reduces cutting forces and frictional heat while improving machining efficiency and surface quality. Ultrasonic-assisted machining finds widespread application in processing hard and brittle materials like ceramics, glass, and composites, offering an effective means to enhance processing efficiency and quality.

An ultrasound-assisted grinding testbed was constructed to analyze the influence of different processing parameter combinations and each processing factor, aiming to optimize the parameter combination. The testbed is illustrated in Figure 1. Comprising a vertical machining center, a wireless transmission device, an ultrasonic tool holder, a longitudinaltorsional ultrasonic amplitude bar, and a diamond grinding wheel, the grinding test platform is enhanced by an external

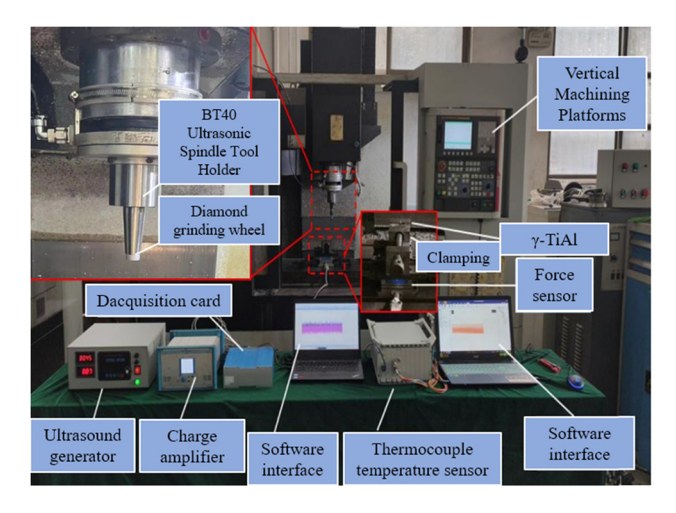


Figure 1: Ultrasound-assisted grinding testbed.

SZ12 intelligent ultrasonic wave generator. This generator enables both longitudinal and torsional ultrasonic vibration of the grinding wheel. Various force signal acquisition devices, including the Kistler 9257B force gauge, the 5070 multi-channel charge amplifier, and the 5697 data acquisition card, are used alongside DynoWare software to capture grinding force values throughout the process. Additionally, for the real-time collection of grinding temperature test data, the DH5933D fast-response thermocouple acquisition instrument and DHDAS dynamic signal acquisition and analysis software are employed.

A diamond grinding wheel, with orderly arranged abrasive grains averaging 115 µm in size, was employed for the experiments. The wheel, measuring 10 mm in width and 20 mm in diameter, was used in conjunction with a workpiece made of y-TiAl intermetallics (Ti-45Al-2Mn-2Nb). The workpiece was 30 mm long in the grinding direction and 15 mm wide radially along the grinding wheel. Its material parameters are detailed in Table 2. Secure clamping to the worktable was ensured using a fixture, while an ultrasound frequency of 35 kHz was employed.

Orthogonal experimental design has been widely used for experimental planning and parameter design due to its effectiveness and simplicity [23]. In this study, an orthogonal table ( $L_{16}$  ( $4^4$ )), as illustrated in Table 3, was established to investigate the influence of grinding parameters on the grinding force and grinding temperature (performance features). The grinding parameters  $a_{\rm p}$ ,  $v_{\rm s}$ , and  $v_{\rm w}$ , as well as the ultrasound amplitude A, varied within the ranges of 2-8  $\mu$ m, 2,000-5,000 rpm, 100-250 mm·min<sup>-1</sup>, and 0-6  $\mu$ m, respectively. Sixteen groups of grinding experiments were conducted in total, with each group of experiments comprising three repetitions. The values obtained were averaged to derive the results.

Table 2: Material properties of y-TiAl intermetallics

| Density<br>(g·cm <sup>−3</sup> ) | Elastic<br>modulus (GPa) | Yield<br>strength (MPa) | Ductility at room temperature (%) | Creep<br>limit (°C) | Antioxidation limit (°C) |  |
|----------------------------------|--------------------------|-------------------------|-----------------------------------|---------------------|--------------------------|--|
| 3.7-3.9                          | 160–176                  | 450-630                 | 1–4                               | 1,000               | 900-1,000                |  |

## 3 Analysis of grinding force and grinding temperature of γ-TiAl intermetallics using ultrasound-assisted grinding

This section analyzes the results of ultrasonic-assisted grinding of  $\gamma$ -TiAl intermetallic compounds and introduces the process steps of GRA. Based on this foundation, the optimization of the ultrasonic-assisted grinding parameters for  $\gamma$ -TiAl intermetallic compounds is conducted using GRA.

Ultrasound-assisted grinding experiments were conducted based on the control variables outlined in Table 3, which include the wheel speed ( $\nu_s$ ), feed rate ( $\nu_w$ ), depth of grinding ( $a_p$ ), and ultrasonic amplitude (A). The outcomes of these experiments are presented in Table 4.

3.1 **GRA** 

GRA is a multivariate correlation analysis method used to handle situations where data are incomplete, or uncertainty are high. This method assesses the degree of correlation between variables by observing the developmental trends of data sequences, thereby evaluating their impact on specific factors [30]. Initially developed by Chinese scholar Li Changyu, GRA was first applied in the field of engineering and later expanded to various domains such as economics, management, and medicine. The target audience for this method includes engineering technicians, managers, economists, and medical researchers. They can use this approach to better understand the correlation between data and provide a scientific basis for decision-making. The

**Table 4:** Values of grinding forces and grinding temperature in ultrasound-assisted grinding experiments

| Serial no. | Α | В | С | D | F <sub>n</sub> (N) | F <sub>t</sub> (N) | T (°C) |
|------------|---|---|---|---|--------------------|--------------------|--------|
| 1          | 1 | 1 | 1 | 1 | 6.07               | 2.79               | 200    |
| 2          | 1 | 2 | 2 | 2 | 8.41               | 4.15               | 205    |
| 3          | 1 | 3 | 3 | 3 | 6.68               | 3.53               | 209    |
| 4          | 1 | 4 | 4 | 4 | 3.22               | 1.08               | 174    |
| 5          | 2 | 1 | 2 | 3 | 13.79              | 7.36               | 225    |
| 6          | 2 | 2 | 1 | 4 | 8.39               | 2.72               | 195    |
| 7          | 2 | 3 | 4 | 1 | 15.41              | 7.93               | 239    |
| 8          | 2 | 4 | 3 | 2 | 15.98              | 6.79               | 230    |
| 9          | 3 | 1 | 3 | 4 | 7.02               | 4.72               | 216    |
| 10         | 3 | 2 | 4 | 3 | 16.99              | 8.66               | 237    |
| 11         | 3 | 3 | 1 | 2 | 13.82              | 8.41               | 240    |
| 12         | 3 | 4 | 2 | 1 | 11.55              | 4.73               | 243    |
| 13         | 4 | 1 | 4 | 2 | 15.59              | 6.09               | 241    |
| 14         | 4 | 2 | 3 | 1 | 17.88              | 9.16               | 268    |
| 15         | 4 | 3 | 2 | 4 | 10.5               | 4.75               | 221    |
| 16         | 4 | 4 | 1 | 3 | 9.14               | 3.37               | 218    |

advantage of GRA lies in its ability to effectively deal with incomplete or highly uncertain data, offering a powerful tool for research and applications across different fields [31].

A gray system is characterized by having both known and unknown information, leading to uncertainty about the relationships between factors within the system. The first step in GRA involves determining the signal-to-noise ratio (SNR) to be optimized, which can fall into three scenarios [32]:

- 1) The smaller the value, the better.
- 2) The larger the value, the better.
- 3) The more standardized the value, the better.

In the context of our experiments aiming to minimize the grinding force and grinding temperature, we aimed to

Table 3: Levels of control variables of the ultrasound-assisted grinding experiments

| Symbol | Control variable                       | Level 1 | Level 2 | Level 3 | Level 4 | Degree of freedom (DOF) |
|--------|--|---------|---------|---------|---------|-------------------------|
| Α      | $a_{\rm p}$ (µm)                       | 2       | 4       | 6       | 8       | 3                       |
| В      | v <sub>s</sub> (rpm)                   | 2,000   | 3,000   | 4,000   | 5,000   | 3                       |
| C      | ν <sub>w</sub> (mm·min <sup>−1</sup> ) | 100     | 150     | 200     | 250     | 3                       |
| D      | A (μm)                                 | 0       | 2       | 4       | 6       | 3                       |

minimize SNR, aligning with scenario (1), where smaller values are preferable. Therefore, the comparison sequence selected in this article is [6.07, 1.08, 174]. This approach was adopted to identify the optimal parameter combination that would effectively reduce both the grinding force and grinding temperature. The minimization of SNR can be represented as follows [33]:

$$\eta_{ij} = -10 \lg \left( \frac{1}{n} \sum_{k=1}^{n} y_{ik}^{2} \right), \tag{1}$$

where  $\eta_{ii}$  is the *j*th SNR in the *i*th group of experiments;  $y_{ik}$ is the result of the kth repeated experiment in the ith group; and *n* is the number of repeated experiments under the same processing conditions and taken as 3.

In GRA, normalizing the data is essential to remove the influence of varying dimensions and magnitudes among different variables. This ensures uniform scales and weights for all variables, thereby improving the accuracy and reliability of the analysis. The primary objective of normalization is to render the variables comparable by mitigating the effects of dimensions and magnitudes, facilitating a more precise evaluation of their correlation [34].

The indicator data were dimensionalized to give a more realistic reflection of the relationship between the data. The expression for the dimensionalization is [33]

$$x_{ij} = \frac{\max_{j} \eta_{ij} - \eta_{ij}}{\max_{j} \eta_{ij} - \min_{j} \eta_{ij}},$$
 (2)

where  $x_{ij}$  is the result of the jth repeated performance test in the *i*th group of experiments.

Deng's GRA model stands as one of the earliest models for calculating the grey relational grade, rooted in gray system theory [25]. This model adheres to the four axioms of GRA and emphasizes the impact of the distance between two points on the relational degree. The gray relational coefficient (GRC) is estimated as follows [32]:

$$\zeta_{ij} = \frac{\min_{i} \min_{j} \Delta_{ij} + \zeta \max_{i} \max_{j} \Delta_{ij}}{\Delta_{ij} + \zeta \max_{i} \max_{j} \Delta_{ij}},$$
(3)

$$\Delta_{ii} = |x_i^0 - x_{ii}|, \tag{4}$$

where  $\xi_{ij}$  is the GRC;  $\Delta_{ij}$  is the difference between  $x_i^0$  and  $x_{ij}$ ;  $x_i^0$  is the optimal sequence of the *i*th variable; and  $\zeta$  is the discrimination coefficient defined in the interval [0, 1]. The smaller the value of  $\zeta$ , the greater the difference between the discrimination coefficients and the higher the differentiating ability [35]. In this study, the same weight is assigned to the responses, and so the value of  $\zeta$  is 0.5. The gray relational grade is determined from the GRC corresponding to each quality feature, as follows [28,34]:

$$\gamma_j = \frac{1}{m} \sum_{i=1}^m \beta_i \zeta_{ij},\tag{5}$$

$$\sum_{i=1}^{m} \beta_i = 1,\tag{6}$$

where  $y_i$  is the gray relational grade for the *j*th experiment;  $\beta_i$  is the weight of the *i*th response factor; *m* is the number of performance features and is taken as 3. Therefore,  $y_i$ represents the gray relational grade between the reference sequence and the comparability sequence.

Figure 2 illustrates the overall process of GRA. The optimization steps for the grinding forces  $F_t$  and  $F_n$  and the grinding temperature *T* are as follows:

- 1) Convert the experimental result into SNR using Eq. (1).
- 2) Normalize SNR using Eq. (2).
- 3) Calculate the GRC using Eqs. (3) and (4).
- 4) Calculate the gray relational degree (GRD) using Eq. (5).
- 5) Obtain the optimized grinding parameters.

### 3.2 Optimization results using GRA

The data of grinding forces and grinding temperature were processed using the method described in Section 3.1. The calculated values of SNR and GRC are presented in Table 5.

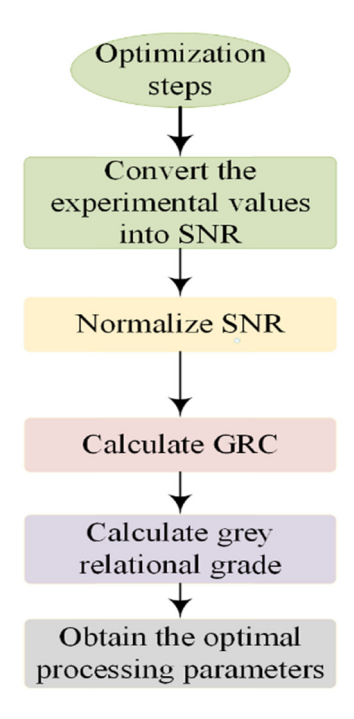


Figure 2: Overall process of GRA.

It can be observed from the data that among the 16 groups of values, the maximum GRD was 1.633, obtained from experiment No. 4. Hence, the best grinding effect was achieved with the grinding parameter combination  $A_1B_4C_4D_4$ . That is,  $a_p = 2 \mu m$ ,  $\nu_s = 5,000 \text{ rpm}$ , and  $\nu_w = 250 \text{ mm} \cdot \text{min}^{-1}$ , corresponding to which  $F_n = 3.22 \text{ N}$ ,  $F_t = 1.08 \text{ N}$ , and  $T = 174 ^{\circ}\text{C}$ .

Table 6 displays the average GRD values of all parameter levels. The GRD values for each factor were summed across each column, and then the average was calculated. It is noticeable that  $a_{\rm p}$  had the highest grey relational grade, whereas  $v_{\rm w}$  had the lowest gray relational grade. Regarding the grinding effect, the grinding depth  $(a_{\rm p})$  had the most significant impact, while the grinding wheel speed  $(v_{\rm w})$  had the least impact.

### 4 Surface integrity analysis of the y-TiAl intermetallics after ultrasound-assisted grinding

Through GRA, the optimal processing parameters and the relative influence of each parameter on the processing effect of ultrasonic-assisted grinding of  $\gamma$ -TiAl intermetallic compounds were determined. However, the individual impact of each processing parameter on the processing effect remains unknown. Therefore, it is necessary to conduct an analysis of the effects of different processing parameters on the processing quality of  $\gamma$ -TiAl intermetallic compounds.

Table 6: Average responses of GRD

|                | Level 1 | Level 2 | Level 3 | Level 4 | Max-min | Rank |
|----------------|---------|---------|---------|---------|---------|------|
| $a_{\rm p}$    | 1.186   | 0.898   | 0.852   | 0.849   | 0.336   | 1    |
| V <sub>s</sub> | 0.931   | 0.905   | 0.885   | 1.064   | 0.179   | 3    |
| $v_{\rm w}$    | 0.914   | 0.901   | 0.886   | 1.013   | 0.128   | 4    |
| Α              | 0.864   | 0.864   | 0.908   | 1.078   | 0.214   | 2    |

### 4.1 Surface roughness analysis

The Olympus 3D measurement laser microscope, model OLS5100, was selected to extract and compute three-dimensional surface roughness data from  $\gamma$ -TiAl intermetallic compound specimens. To ensure precise results and minimize interference from surface impurities, the specimens underwent thorough cleaning with an ultrasonic cleaner before measurement. Recognizing the inherent randomness in individual sampling, a method was developed to improve the accuracy of obtaining three-dimensional roughness values. As depicted in Figure 3, three random areas within each specimen were sampled, where surface roughness values were then extracted. Finally, the arithmetic mean of these values was calculated to yield a more reliable final result.

The term  $D_R$  was introduced to describe the improving effect of ultrasonic vibration for grinding force under the same processing parameters and to discuss the extent to which the imposed ultrasonic vibration reduces surface roughness.  $D_R$  is given by

Table 5: SNR and gray relational grade for the grinding forces and grinding temperature

| Serial no. |                    | SNR value          |         | Din                | nensionalized      | SNR    |                    | GRD                |               |       |
|------------|--------------------|--------------------|---------|--------------------|--------------------|--------|--------------------|--------------------|---------------|-------|
|            | F <sub>n</sub> (N) | F <sub>t</sub> (N) | T (°C)  | F <sub>n</sub> (N) | F <sub>t</sub> (N) | T (°C) | F <sub>n</sub> (N) | F <sub>t</sub> (N) | <i>T</i> (°C) |       |
| 1          | -15.664            | -8.912             | -46.021 | 0.308              | 0.359              | 0.000  | 0.575              | 0.457              | 2.244         | 1.092 |
| 2          | -18.496            | -12.361            | -46.235 | 0.636              | 0.550              | 0.155  | 0.472              | 0.368              | 2.167         | 1.002 |
| 3          | -16.496            | -10.955            | -46.403 | 0.818              | 0.830              | 0.348  | 0.540              | 0.399              | 2.110         | 1.017 |
| 4          | -10.157            | -0.668             | -44.811 | 0.465              | 0.506              | 0.195  | 1.000              | 1.094              | 2.804         | 1.633 |
| 5          | -22.791            | -17.338            | -47.044 | 0.725              | 0.830              | 0.344  | 0.371              | 0.287              | 1.919         | 0.859 |
| 6          | -18.475            | -8.691             | -45.801 | 0.834              | 0.956              | 0.582  | 0.472              | 0.464              | 2.328         | 1.088 |
| 7          | -23.756            | -17.985            | -47.568 | 0.612              | 0.627              | 0.321  | 0.354              | 0.279              | 1.786         | 0.806 |
| 8          | -24.072            | -16.637            | -47.235 | 0.924              | 0.886              | 0.368  | 0.349              | 0.296              | 1.869         | 0.838 |
| 9          | -16.927            | -13.479            | -46.689 | 1.000              | 1.000              | 0.894  | 0.524              | 0.346              | 2.020         | 0.963 |
| 10         | -24.604            | -18.750            | -47.495 | 0.000              | 0.111              | 0.070  | 0.340              | 0.270              | 1.804         | 0.805 |
| 11         | -22.810            | -18.496            | -47.604 | 0.206              | 0.428              | 0.211  | 0.370              | 0.273              | 1.778         | 0.807 |
| 12         | -21.252            | -13.497            | -47.712 | 0.308              | 0.590              | 0.396  | 0.402              | 0.345              | 1.753         | 0.833 |
| 13         | -23.857            | -15.692            | -47.640 | 0.078              | 0.406              | 0.426  | 0.352              | 0.309              | 1.770         | 0.810 |
| 14         | -25.047            | -19.238            | -48.563 | 0.465              | 0.627              | 0.459  | 0.333              | 0.264              | 1.580         | 0.726 |
| 15         | -20.424            | -13.534            | -46.888 | 0.682              | 0.793              | 0.634  | 0.420              | 0.345              | 1.962         | 0.909 |
| 16         | -19.219            | -10.553            | -46.769 | 0.078              | 0.377              | 0.371  | 0.451              | 0.410              | 1.996         | 0.952 |

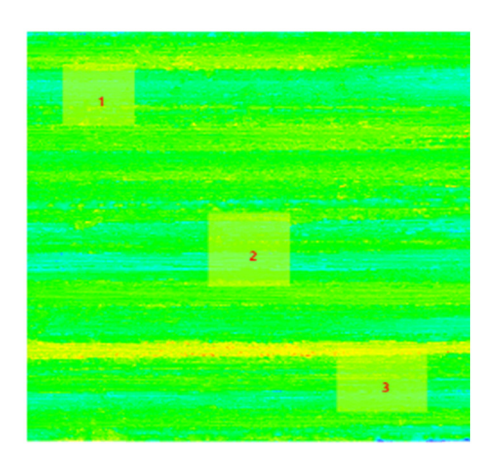


Figure 3: Sampling position.

$$D_{\rm R} = \frac{(R_{\rm CG} - R_{\rm UAG})}{R_{\rm CG}} \times 100\%. \tag{7}$$

### 4.1.1 Influence of grinding depth on surface roughness

Figure 4 illustrates the variation trend of surface roughness Ra as the grinding depth  $a_{\rm p}$  varies, with and without ultrasonic vibration under  $v_{\rm s}=4,000\,{\rm rpm}$  and  $v_{\rm w}=150\,{\rm mm\cdot min^{-1}}$ . The figure demonstrates that as the grinding depth  $a_{\rm p}$  increased, the surface roughness Ra of the  $\gamma$ -TiAl intermetallics also increased. This phenomenon arises because a greater grinding depth leads to an increase in the maximum undeformed chip thickness of a single abrasive grain. Consequently, the normal grinding force increases, resulting in a significant increase in heat generation during grinding. This heightened plastic uplift deformation on the surface of the  $\gamma$ -TiAl intermetallics exacerbates

surface roughness. Additionally, the intensified grinding force causes a more pronounced vibration of the grinding wheel, negatively impacting the workpiece quality.

Furthermore, the comparison of surface roughness with and without ultrasonic vibration under identical processing conditions in Figure 4 reveals that ultrasonic vibration reduces the surface roughness of the processed workpiece. This reduction occurs because ultrasonic vibration extends the movement trajectory, leading to an increased maximum undeformed chip thickness of a single abrasive grain and improving the workpiece grinding quality. Additionally, ultrasonic vibration induces an overlap of movement trajectories of several abrasive grains, leading to repeated grinding at the same positions on the workpiece surface and further decreasing surface roughness.

In Figure 4, the orange line signifies the reduction in surface roughness due to ultrasonic vibration at varying grinding depths. Notably, as the grinding depth increases, surface roughness gradually decreases. However, when the grinding depth reaches 8  $\mu m$ , the surface roughness decreases by only 8.89%. This analysis indicates that the grinding depth also plays a role in attenuating the reduction in surface roughness.

### 4.1.2 Influence of grinding wheel speed on surface roughness

Figure 5 illustrates the impact of grinding wheel speed on surface roughness Ra. It is evident from Figure 4 that with other parameters held constant, the surface roughness of the workpiece gradually decreased as the grinding wheel speed increased. This phenomenon occurs because as the

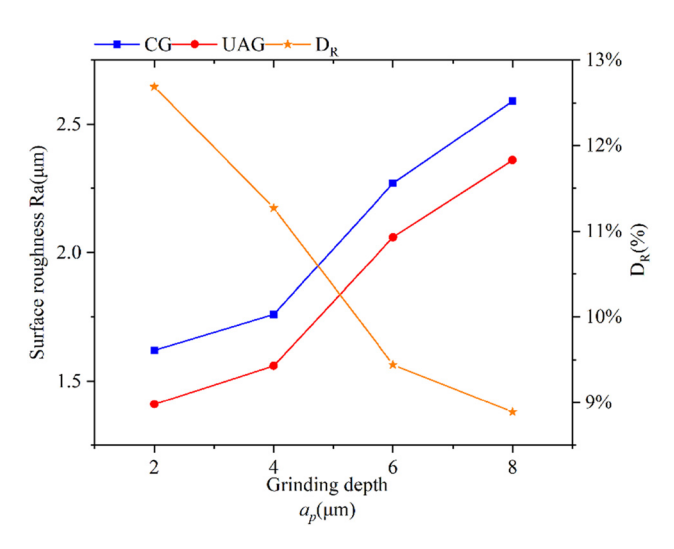


Figure 4: Influence of the grinding depth on surface roughness Ra.

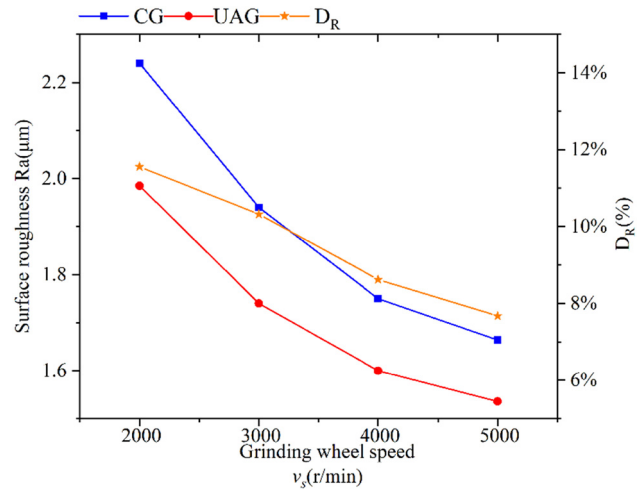


Figure 5: Influence of grinding wheel speed on surface roughness Ra.

S — Song Yang et al. DE GRUYTER

grinding wheel speed increases, the chip thickness of a single abrasive grain decreases while the instantaneous number of effective abrasive grains engaged in grinding per unit time increases. Consequently, the texture density on the workpiece surface increases, and the spacing between cutting trajectories narrows. Moreover, the plastic deformation and uplift height on the groove's two sides decreases, reducing the surface roughness of the workpiece. However, when the grinding wheel speed reached 4,000 rpm, the rate of decrease in surface roughness became significantly smaller. This result can be attributed to lowand high-frequency forced self-excited vibrations in the grinding process system due to excessively high grinding wheel speed, which compromises system stability. These vibrations lead to an increase in the wave crest's height and trough depth on the workpiece surface. Nonetheless, the specific impact degree may vary depending on the type of machine tool used.

Additionally, it is observed from Figure 5 that after ultrasonic vibration was applied, the surface roughness decreased under the same process parameters. This observation aligns with the explanation for reduced surface roughness under ultrasonic vibration discussed in the previous section. Furthermore, as the grinding wheel speed increased, the rate of decrease in surface roughness became progressively smaller under ultrasonic vibration. This suggests that a higher grinding wheel speed under ultrasonic vibration weakens the beneficial effect of ultrasonic vibration on surface roughness improvement. As mentioned in Section 4, a higher grinding wheel speed also diminishes the positive effect of ultrasonic vibration on the grinding force. Thus, it can be inferred that a higher grinding wheel speed has a negative impact on the efficacy of ultrasonic vibration in enhancing grinding performance.

### 4.1.3 Influence of feed speed on surface roughness

Figure 6 illustrates the influence of feed speed on surface roughness Ra. It is evident from Figure 6 that with other parameters held constant, surface roughness increased significantly as the feed speed increased, whether during ultrasound-assisted grinding or conventional grinding. This increase occurs because a higher feed speed leads to a greater material removal amount of the workpiece per unit time. Consequently, with the number of abrasive grains engaged in grinding remaining constant, the grinding force experienced by a single abrasive grain increases. This results in an increased uplift height on the two sides of the groove, deteriorating the grinding quality. Based on the influence of feed speed on the grinding force, a lower feed speed is preferable during

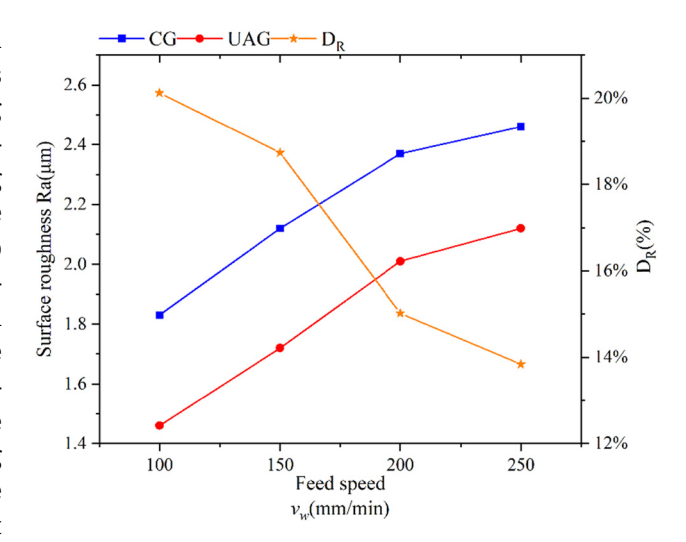


Figure 6: Influence of feed speed on surface roughness Ra.

ultrasound-assisted grinding to reduce processing difficulty and improve the surface grinding quality of the workpiece.

Furthermore, as indicated by the variation law of  $D_R$  in Figure 6,  $D_R$  (degree of reduction) decreased gradually as the feed speed increased. This analysis suggests that a higher feed speed hampers the beneficial effect of ultrasonic vibration on the grinding quality of the workpiece. The reason for this is that a higher feed speed diminishes the overlap interference between adjacent abrasive grains in the grinding arc zone, significantly impairing the performance of repeated grinding by adjacent abrasive grains.

### 4.2 Surface morphology of the workpiece

Surface morphology and profile height of the machined surface serve as direct indicators of the interaction between abrasive grains and the  $\gamma$ -TiAl intermetallics, reflecting the material removal mode of the workpiece and considered crucial indicators of workpiece surface quality. The surface morphology and profile of the workpiece were analyzed using the Olympus OLS5100 3D Laser Scanning Microscope.

Figure 7 displays the surface morphology and profile height curves of the  $\gamma$ -TiAl intermetallic workpieces obtained through ultrasound-assisted grinding and conventional grinding, with the ultrasound amplitude set at A=4 µm. The average  $\Delta h$ , defined as the difference in the profile height between ultrasound-assisted grinding and conventional grinding, signifies the effectiveness of ultrasonic vibration in reducing the surface profile height. A larger  $\Delta h$  indicates better performance of ultrasound-assisted grinding in improving the surface quality.

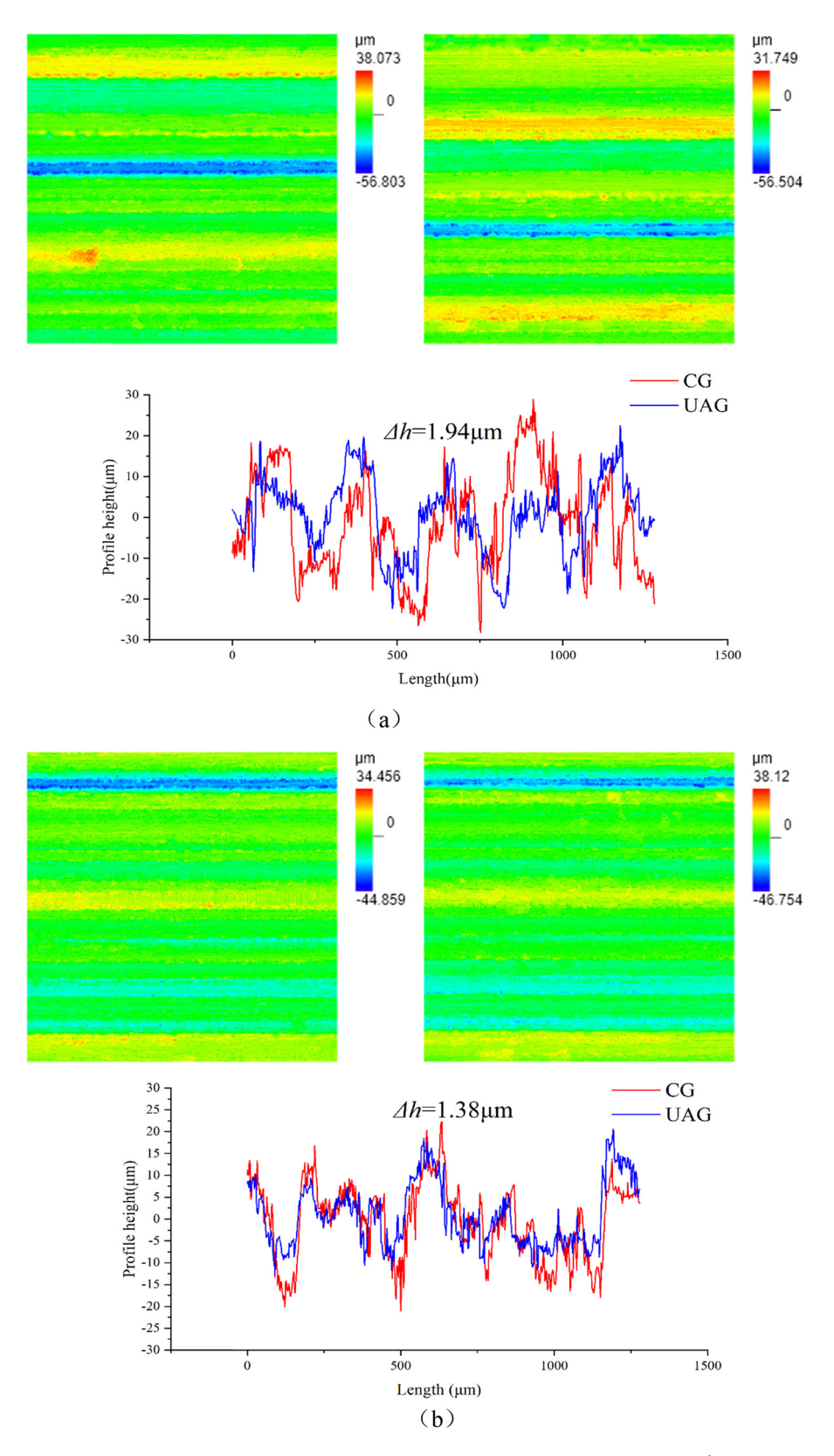


**Figure 7:** Surface morphology and profile of the workpiece. (a)  $a_p = 4 \, \mu m$ ,  $v_s = 4,000 \, \text{rpm}$ , and  $v_w = 150 \, \text{mm} \cdot \text{min}^{-1}$ . (b)  $a_p = 6 \, \mu m$ ,  $v_s = 4,000 \, \text{rpm}$ , and  $v_{\rm w}$  = 150 mm·min<sup>-1</sup>. (c)  $a_{\rm p}$  = 4  $\mu$ m,  $v_{\rm s}$  = 5,000 rpm, and  $v_{\rm w}$  = 150 mm·min<sup>-1</sup>. (d)  $a_{\rm p}$  = 4  $\mu$ m,  $v_{\rm s}$  = 4,000 rpm, and  $v_{\rm w}$  = 200 mm·min<sup>-1</sup>.

**10** — Song Yang et al.

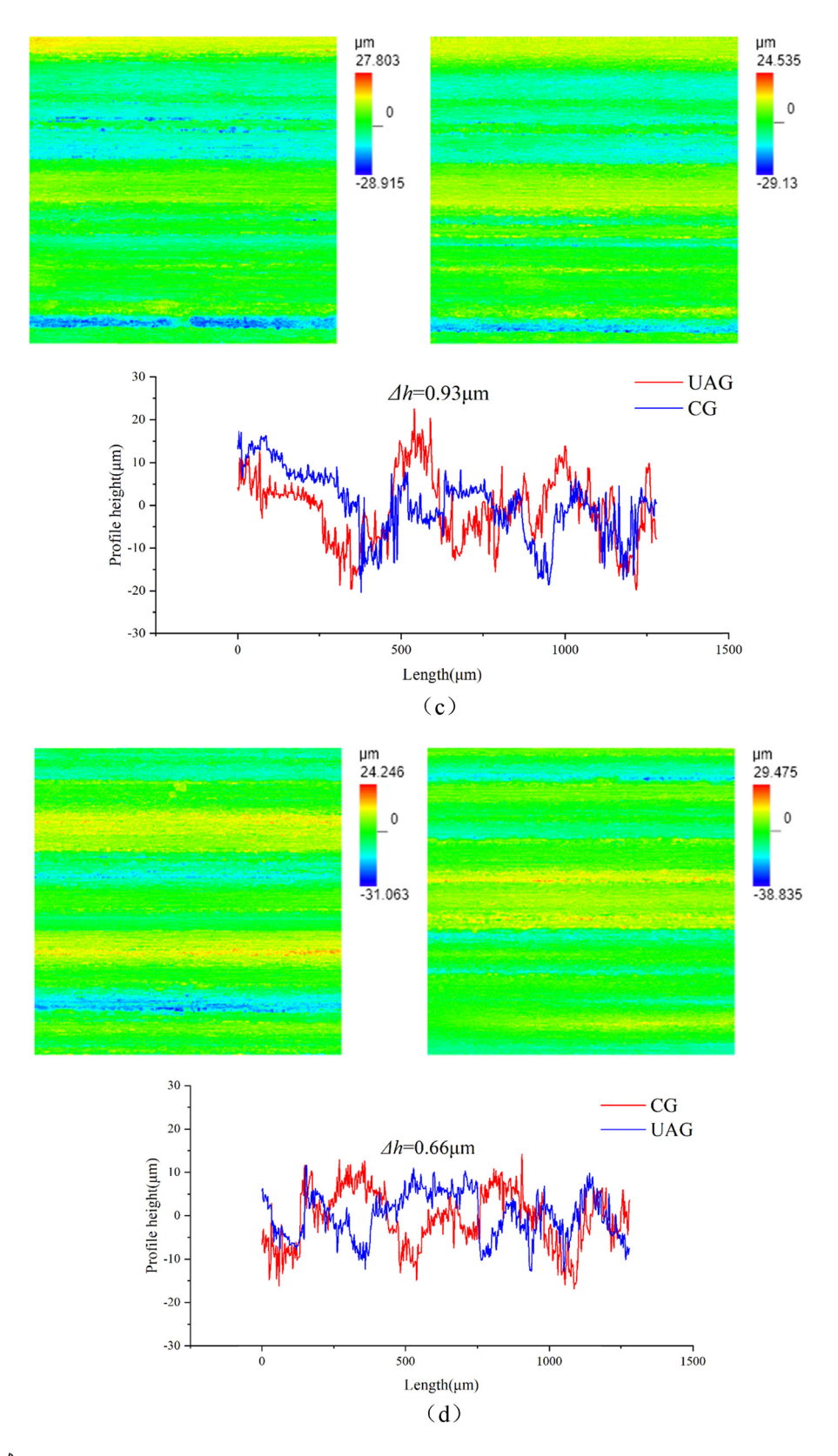


Figure 7: (Continued)

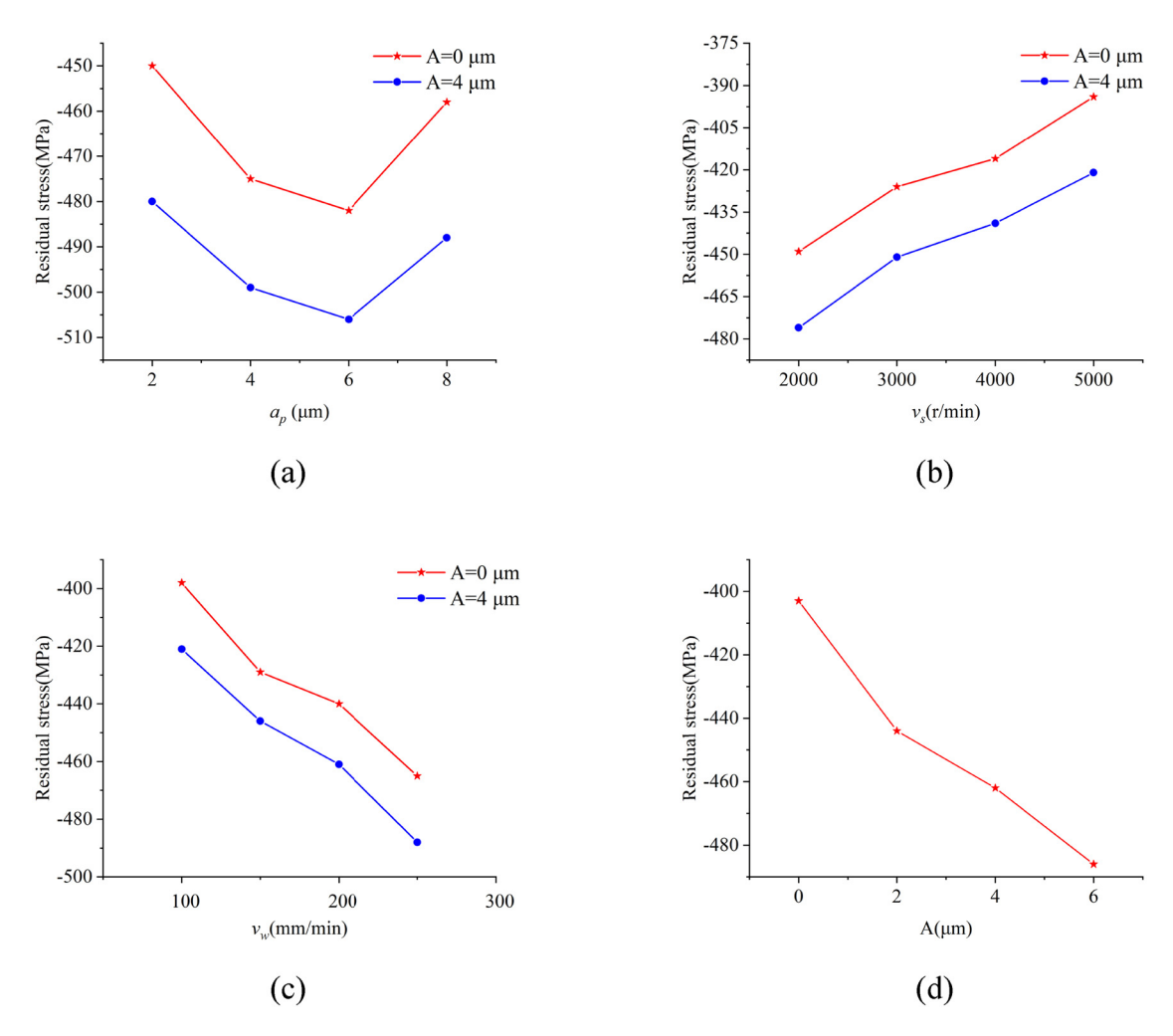
Figure 7(a) shows the surface morphology and the height of the surface profile with and without ultrasonic vibration at  $a_{\rm p}$  = 4 µm,  $\nu_{\rm s}$  = 4,000 rpm, and  $\nu_{\rm w}$  = 150 mm·min<sup>-1</sup>. As depicted in Figure 7, the average height of the surface profile of the workpiece subjected to ultrasonic vibration decreased by 1.94 µm compared to conventional grinding. These results indicate that ultrasound-assisted grinding led to a reduction in the surface profile height compared to ordinary grinding, resulting in a more uniform profile height along the vibration direction. This improvement occurred because the scratches created by abrasive grains during ultrasound-assisted grinding interfered with and complemented each other. Consequently, the surface textures became densely interwoven, enhancing profile precision.

Figure 7(b) shows the surface morphology and the height of the surface profile with and without ultrasonic vibration at  $a_{\rm p}=6~\mu{\rm m},~v_{\rm s}=4,000~{\rm rpm},~{\rm and}~v_{\rm w}=150~{\rm mm\cdot min^{-1}}.$  Compared with conventional grinding, the average height of the surface profile of the workpiece subjected to ultrasonic vibration

decreased by 1.38  $\mu$ m. This result indicates that as the grinding depth increased, the surface profiles of the work-pieces obtained by ultrasound-assisted grinding and conventional grinding became more consistent. Therefore, increasing the grinding depth would weaken the surface grinding quality of the workpiece subjected to ultrasonic vibration.

As shown in Figure 7(c) and (d), at  $a_{\rm p}=4\,\mu{\rm m}$ ,  $v_{\rm s}=5,000\,{\rm rpm}$ ,  $v_{\rm w}=150\,{\rm mm\cdot min^{-1}}$  and  $a_{\rm p}=4\,\mu{\rm m}$ ,  $v_{\rm s}=4,000\,{\rm rpm}$ , and  $v_{\rm w}=200\,{\rm mm\cdot min^{-1}}$ , the average height of surface profile  $\Delta h$  decreased by 0.93 and 0.66  $\mu{\rm m}$ , respectively, with ultrasonic vibration. Compared with Figure 7(a), it is evident that increasing either the grinding wheel speed or feed speed would diminish the beneficial effect of ultrasonic vibration on the surface quality of the machined workpiece.

An examination of the surface morphology of the  $\gamma$ -TiAl intermetallics workpieces obtained by ultrasound-assisted grinding and conventional grinding revealed that increasing the grinding depth, feed speed, and grinding



**Figure 8:** Residual stresses under different process parameters. (a)  $v_s = 4000 \text{ r/min}$ ,  $v_w = 150 \text{ mm/min}$ ; (b)  $a_p = 4 \text{ µm}$ ,  $v_w = 150 \text{ mm/min}$ ; (c)  $a_p = 4 \text{ µm}$ ,  $v_s = 4000 \text{ r/min}$ ; (d)  $a_p = 4 \text{ µm}$ ,  $v_s = 4000 \text{ r/min}$ ,  $v_w = 150 \text{ mm/min}$ .

wheel speed would all reduce the improving effect of ultrasonic vibration on the surface grinding quality of the workpiece. Simultaneous analysis of the influence of process parameters on the grinding force and surface roughness indicated that altering the process parameters did indeed impact the grinding performance to a certain extent.

### 4.3 Residual stress on the workpiece surface

Residual stresses on the processed surface of the workpiece were examined in this study using a PROTO-produced X-ray diffractometer. The grinding process results in significantly higher "compressive" residual stresses perpendicular to the grinding feed direction compared to those along the feed direction. Consequently, residual compressive stresses are lower along the grinding direction. Recognizing that greater residual compressive stresses enhance the workpiece's fatigue resistance and service life, the detection of residual stresses was carried out along the workpiece feed direction, following the principle of the "barrel effect," wherein the strength of a barrel is determined by its shortest stave.

The results presented in Figure 8 reveal that, within the examined range of process parameters, the residual stress on the workpiece surface consistently maintained a compressive state throughout the experiments. Furthermore, Figure 8(a)-(c) demonstrates that ultrasonic vibration induces an augmentation in residual compressive stress on the workpiece surface post-processing. This augmentation is attributed to the application of ultrasonic vibration, which fosters additional compressive interactions between abrasive grains and the workpiece surface, thereby reinforcing the residual compressive stress on the workpiece surface. A detailed analysis of Figure 8(a) revealed that as the grinding depth increased, the residual compressive stress on the workpiece surface followed a pattern of first increasing and then decreasing. This trend is attributed to the increasing grinding force with higher grinding depths, leading to a gradual increase in the residual compressive stress in the grinding zone. Concurrently, as the material removal rate per unit time increased, the grinding temperature also increased. However, due to the lower linear speed of the grinding wheel used in the experiments, the heat generation and accumulation during grinding were limited. Consequently, under shallower grinding depths, the grinding force had a more pronounced impact on residual stress compared to heat generation. Ultrasonic vibration interrupted the cutting action at high frequencies, reducing the net material removal volume and limiting temperature increase. However, when the grinding depth exceeded 6 µm, the residual compressive

stress decreased due to increased contact arc length and contact time, leading to a sharp temperature increase and subsequent thermoplastic deformation.

According to Figure 8(b), as the grinding wheel speed increased, the residual compressive stress on the workpiece surface gradually decreased. This reduction is attributed to decreased grinding force and temperature, leading to lower residual compressive stress caused by mechanical stress. However, increased grinding wheel speed also elevated grinding temperature, contributing to higher residual compressive stress from thermal stress. Therefore, the overall reduction in residual stress can be attributed to the mechanical-thermal coupling effect.

Figure 8(c) indicates that increasing the feed speed led to higher residual compressive stress on the workpiece surface. This increase is due to the larger chip thickness, resulting in higher material removal and increased contact area and friction. However, the shortened duration of heat exposure and reduced heat flux mitigated thermoplastic deformation, leading to a decrease in residual compressive stress.

As shown in Figure 8(d), increasing the ultrasound amplitude resulted in higher residual compressive stress on the workpiece surface. This is because the machined surface was more prone to rebound during grinding, leading to intense squeeze friction and higher residual compressive stress. However, ultrasound-assisted grinding reduced grinding force and temperature, with higher amplitudes leading to greater separation between abrasive grains and workpieces, reducing residual tensile stress from thermal effects. Yet, increased amplitude also intensified abrasive grain contact with the workpiece, elevating residual compressive stress significantly.

Overall, these findings highlight the intricate interplay of process parameters and their effects on residual stress in y-TiAl intermetallic workpieces during grinding operations.

### 5 Discussion

The machining of  $\gamma$ -TiAl intermetallics, known for their challenging machinability, is crucial in producing aircraft engine components. This study investigated their machinability through ultrasonic-assisted grinding experiments, meticulously examining various parameters: grinding wheel speed ( $\nu_{\rm s}$ ), feed speed ( $\nu_{\rm w}$ ), grinding depth ( $a_{\rm p}$ ), and ultrasound amplitude (A), to understand their influence on grinding force and temperature. GRA and analysis of variance aided in a comprehensive analysis of the experimental data. Post-processing evaluation focused on surface integrity, including surface roughness, morphology, and residual stress.

The findings emphasize the pivotal role of grinding depth  $(a_n)$  in significantly impacting both grinding force and temperature, highlighting its importance in the machining process. Conversely, the effect of grinding wheel speed  $(v_w)$  was relatively minor. Introducing ultrasonic vibration emerged as a promising technique to enhance grinding quality, resulting in a remarkable reduction in surface roughness of up to 20.12%. Remarkably, residual stress observed on the workpiece surface remained predominantly compressive throughout the experiments, fluctuating between a maximum of 486 MPa and a minimum of 394 MPa.

In essence, this study provides crucial insights into the machinability of y-TiAl intermetallics, revealing the efficacy of ultrasonic-assisted grinding and the nuanced interplay between grinding parameters and surface integrity. These findings have significant implications for the aerospace industry, offering valuable guidance for optimizing machining processes and improving the performance of y-TiAl intermetallics components in aircraft engine manufacturing

### 6 Conclusions

Ultrasound-assisted grinding experiments were conducted using a diamond grinding wheel with carefully arranged abrasive grains. GRA and analysis of variance were employed to analyze the impact of grinding parameters on the grinding properties of titanium-aluminum intermetallic workpieces. The integrity and quality of the machined surface were meticulously assessed. Based on the experimental results, we arrived at the following conclusions:

- 1) Based on GRA, the optimal grinding parameter combination was determined as  $a_p = 2 \mu m$ ,  $v_s = 5,000 \text{ rpm}$ , and  $v_{\rm w}$  = 250 mm·min<sup>-1</sup>, which corresponded to  $F_{\rm n}$  = 3.22 N,  $F_t = 1.08 \text{ N}$ , and  $T = 174 ^{\circ}\text{C}$ . Notably, grinding depth exerted the most significant influence on both grinding force and temperature, while the grinding wheel speed  $(v_w)$  had the least impact among all parameters studied.
- 2) The surface roughness (Ra) of the workpiece increased with higher feed speeds and grinding depths but decreased as the grinding wheel speed increased. Ultrasonic vibration notably reduced Ra, with reductions ranging from 7.67 to 20.12%. However, increased grinding wheel speed, grinding depth, and feed speed countered the beneficial effects of ultrasonic vibration on Ra.
- 3) Ultrasonic vibration effectively reduced the surface profile height of the workpiece, with reductions ranging from 0.66 to 1.94 µm within the selected ultrasound amplitude values. However, a higher grinding depth and feed speeds led to smaller reductions in the profile height (1.38, 0.93, and 0.66 µm, respectively).

4) Throughout the experiments, the residual stress on the workpiece surface remained compressive. Its magnitude increased with higher grinding wheel speeds and ultrasound amplitudes but decreased with increased grinding wheel speed. Residual stress initially increased with increased grinding depth, peaking at 482 MPa before decreasing to 458 MPa.

Acknowledgments: The authors are thankful for the financial support from the National Natural Science Funds of China (U1904170) and the Opening Project of the Key Laboratory of Precision Manufacturing Technology and Engineering, Henan Polytechnic University.

Funding information: This study was supported by financial support from the National Natural Science Funds of China (U1904170) and the Opening Project of the Key Laboratory of Precision Manufacturing Technology and Engineering, Henan Polytechnic University.

Author contributions: Song Yang and Guoging Xiao organized and conceived the project, analyzed, and arranged data. Guoqing Xiao conducted the experiments, and Guangjin Zhang assisted in the analysis through constructive discussions. All authors have accepted responsibility for the entire content of this manuscript and approved its submission.

**Conflict of interest:** The authors state no conflict of interest.

Data availability statement: The datasets generated and/ or analyzed during the current study are available from the corresponding author on reasonable request.

### References

- Kim, Y. K., J. K. Hong, and K. A. Lee. Enhancing the creep resistance [1] of electron beam melted gamma Ti-48Al-2Cr-2Nb alloy by using two-step heat treatment. Intermetallics, Vol. 121, 2020, id. 106771.
- Pan, H. P., K. P. Zhang, J. M. Chen, X. Y. Zhang, H. Zhao, and R. Hu. Variant selection of massive y subgrains and corresponding mechanical properties in Ta containing y-TiAl-based alloys. Materials Letters, Vol. 333, 2023, id. 133689.
- [3] Cui, X. P., H. Ding, Y. Y. Zhang, Y. Yao, G. H. Fan, L. J. Huang, et al. Fabrication, microstructure characterization and fracture behavior of a unique micro-laminated TiB-TiAl composites. Journal of Alloys and Compounds, Vol. 775, 2019, pp. 1057-1067.
- [4] Xia, Z. W., C. W. Shan, M. H. Zhang, M. C. Cui, and M. Luo. Machinability of y-TiAl: A review. Chinese Journal of Aeronautics, Vol. 36, No. 7, 2023, pp. 40-75.
- Li, Z. H., S. Yang, X. N. Liu, G. Q. Xiao, H. Z. San, Y. Z. Zhang, et al. [5] Grinding force model for ultrasonic assisted grinding of y-TiAl intermetallic compounds and experimental validation. Reviews on Advanced Materials Science, Vol. 63, No. 1, 2024, id. 20230167.

- [6] Xia, Z. W., C. W. San, M. H. Zhang, W. G. Liu, M. C. Cui, and M. Luo. Machinability of elliptical ultrasonic vibration milling y-TiAl: Chip formation, edge breakage, and subsurface layer deformation. *Chinese Journal of Aeronautics*, 2024. [in press].
- [7] Genc, O. and R. Unal. Development of gamma titanium aluminide (γ-TiAl) alloys: A review. *Journal of Alloys and Compounds*, Vol. 929, 2022. id. 167262.
- [8] Xu, R. R., M. Q. Li, and Y. H. Zhao. A review of microstructure control and mechanical performance optimization of y-TiAl alloys. *Journal* of Alloys and Compounds, Vol. 932, 2023, id. 167611.
- [9] Wang, Y., G. F. Gao, K. Zhang, Y. Wang, X. B. Wang, and D. H. Xiang. Modelling of tribological behavior and wear for micro-textured surfaces of Ti2AlNb intermetallic compounds machined with multidimensional ultrasonic vibration assistance. *Tribology International*, Vol. 191, 2024, id. 109167.
- [10] Fan, T., C. Yao, L. Tan, Y. L. Cao, Y. Q. Sun, and W. H. Tang. The influence of induction-assisted milling on the machining characteristics and surface integrity of γ-TiAl alloys. *Journal of Manufacturing Processes*, Vol. 118, 2024, pp. 215–227.
- [11] Hayat, M. D., H. Singh, Z. He, and P. Cao. Titanium metal matrix composites: An overview. *Composites Part A: Applied Science and Manufacturing*, Vol. 121, 2019, pp. 418–438.
- [12] Wu, S. J., F. Y. Chen, D. Z. Wang, G. Q. Wang, C. H. Li, and J. Z. Lu. Machining mechanism and stress model in cutting Ti6Al4V. *The International Journal of Advanced Manufacturing Technology*, Vol. 131, No. 5, 2024, pp. 2625–2639.
- [13] Miao, Q., W. F. Ding, W. J. Kuang, and C. Y. Yang. Comparison on grindability and surface integrity in creep feed grinding of GH4169, K403, DZ408 and DD6 nickel-based superalloys. *Journal of Manufacturing Processes*, Vol. 49, 2020, pp. 175–186.
- [14] Yang, H., J. Xie, Q. P. He, J. H. Liu, and Y. Q. Shi. Study on diamond cuttingto-burnishing for thermal-force dispersion in dry metal grinding. *Journal* of Materials Processing Technology, Vol. 313, 2023, id. 117874.
- [15] Yang, Z. B., D. Y. He, W. Sun, Y. Q. Zhang, S. Y. Zhang, H. B. Shi, et al. Determination of the grinding force on optical glass based on a diamond wheel with an ordered arrangement of abrasive grains. *The International Journal of Advanced Manufacturing Technology*, Vol. 115, 2021, pp. 1237–1248.
- [16] Hood, R., P. Cooper, D. K. Aspinwall, S. L. Sool, and D. S. Lee. Creep feed grinding of γ-TiAl using single layer electroplated diamond superabrasive wheels. CIRP Journal of Manufacturing Science and Technology, Vol. 11, 2015, pp. 36–44.
- [17] Xi, X. X., W. F. Ding, Z. X. Wu, and L. Anggei. Performance evaluation of creep feed grinding of γ-TiAl intermetallics with electroplated diamond wheels. *Chinese Journal of Aeronautics*, Vol. 34, No. 6, 2021, pp. 100–109.
- [18] Chen, T., X. W. Wang, B. Zhao, W. F. Ding, and J. H. Xu. Surface integrity evolution during creep feed profile grinding of γ-TiAl blade tenon. *Chinese Journal of Aeronautics*, 2024. [in press].
- [19] Bhaduri, D., S. L. Soo, D. K. Aspinwall, D. Novovic, S. Bohr, P. Harden, et al. Ultrasonic assisted creep feed grinding of gamma titanium aluminide using conventional and superabrasive wheels. CIRP Annals, Vol. 66, No. 1, 2017, pp. 341–344.
- [20] Liang, Z. Q., S. L. Xiao, H. B. Yu, Q. C. Li, Y. F. Zheng, L. J. Xu, et al. Enhanced high temperature tensile and creep properties of a β-solidified y-TiAl alloy with the hybrid addition of C and Y2O3. *Intermetallics*, Vol. 150, 2022, id. 107698.
- [21] Chen, T., Q. Miao, M. Y. Xiong, X. X. Xi, B. Zhao, C. L. Pu, et al. On the residual stresses of turbine blade root of y-TiAl intermetallic alloys

- induced by non-steady-state creep feed profile grinding. *Journal of Manufacturing Processes*, Vol. 82, 2022, pp. 800–817.
- [22] Wang, X. W., Y. Tang, B. Zhao, T. Chen, W. F. Ding, and J. H. Xu. Grindability of y-TiAl intermetallic compounds during ultrasonic vibration-assisted high efficiency deep grinding process. The. *International Journal of Advanced Manufacturing Technology*, Vol. 128, No. 3–4, 2023, pp. 1127–1138.
- [23] Jamshidi, H. and M. J. Nategh. Theoretical and experimental investigation of the frictional behavior of the tool–chip interface in ultrasonic-vibration assisted turning. *International Journal of Machine Tools and Manufacture*, Vol. 65, 2013, pp. 1–7.
- [24] Yang, Z. Y., P. Zou, L. Zhou, X. Wang, and M. M. Usman. Modeling and experimental analysis of surface topography generation mechanism during ultrasonic vibration-assisted grinding. *Precision Engineering*, Vol. 80, 2023, pp. 30–44.
- [25] Zhao, B., X. C. Guo, W. B. Bie, B. Q. Chang, and C. Y. Zhao. Thermomechanical coupling effect on surface residual stress during ultrasonic vibration-assisted forming grinding gear. *Journal of Manufacturing Processes*, Vol. 59, 2020, pp. 19–32.
- [26] Cao, Y., W. F. Ding, B. Zhao, X. B. Wen, S. P. Li, and J. Z. Wang. Effect of intermittent cutting behavior on the ultrasonic vibration-assisted grinding performance of Inconel718 nickel-based superalloy. *Precision Engineering*, Vol. 78, 2022, pp. 248–260.
- [27] Touqeer, M., S. Jabeen, and R. Irfan. A grey relational projection method for multi attribute decision making based on three trapezoidal fuzzy numbers. *Journal of Intelligent & Fuzzy Systems*, Vol. 38, No. 5, 2020, pp. 5957–5967.
- [28] Manimaran, G. and M. P. Kumar. Multiresponse optimization of grinding AISI 316 stainless steel using grey relational analysis. *Materials and Manufacturing Processes*, Vol. 28, No. 4, 2013, pp. 418–423.
- [29] Liu, W., Z. H. Deng, Y. Y. Shang, and L. L. Wan. Effects of grinding parameters on surface quality in silicon nitride grinding. *Ceramics International*, Vol. 43, No. 1, 2017, pp. 1571–1577.
- [30] Kuo, Y., T. Yang, and G. W. Huang. The use of grey relational analysis in solving multiple attribute decision-making problems. *Computers & industrial engineering*, Vol. 55, No. 1, 2008, pp. 80–93.
- [31] Wei, G. W. Gray relational analysis method for intuitionistic fuzzy multiple attribute decision making. *Expert systems with Applications*, Vol. 38, No. 9, 2011, pp. 11671–11677.
- [32] Pillai, J. U., M. Shunmugavel, M. Thangaraj, M. Goldberg, R. Singh, and G. Littlefair. Effects of machining parameters on enhancing Alpha-Beta Titanium alloy using Taguchi-grey relational analysis for aerospace applications. *Proceedings of the Institution of Mechanical Engineers, Part E: Journal of Process Mechanical Engineering*, Vol. 237, No. 2, 2023, pp. 118–127.
- [33] Chen, T., Y. J. Zhu, X. X. Xi, H. X. Huan, and W. F. Ding. Process parameter optimization and surface integrity evolution in the highspeed grinding of TiAl intermetallics based on grey relational analysis method. The. *International Journal of Advanced Manufacturing Technology*, Vol. 117, No. 9, 2021, pp. 2895–2908.
- [34] Thepsonthi, T. and T. Özel. Multi-objective process optimization for micro-end milling of Ti-6Al-4V titanium alloy. *The International Journal of Advanced Manufacturing Technology*, Vol. 63, 2012, pp. 903–914.
- [35] Chan, J. W. K. and T. K. L. Tong. Multi-criteria material selections and end-of-life product strategy: Grey relational analysis approach. *Materials & Design*, Vol. 28, No. 5, 2007, pp. 1539–1546.